Science Robotics
AAAS

robotics.sciencemag.org/cgi/content/full/4/33/eaax7044/DC1

Supplementary Materials for

Untethered soft robotic matter with passive control of shape morphing and propulsion

Arda Kotikian, Connor McMahan, Emily C. Davidson, Jalilah M. Muhammad, Robert D. Weeks, Chiara Daraio*, Jennifer A. Lewis*

*Corresponding author. Email: daraio@caltech.edu (C.D.); jalewis@seas.harvard.edu (J.A.L.)

Published 21 August 2019, *Sci. Robot.* **4**, eaax7044 (2019)
DOI: 10.1126/scirobotics.aax7044

The PDF file includes:

Other Supplementary Material for this manuscript includes the following:

(available at robotics.sciencemag.org/cgi/content/full/4/33/eaax7044/DC1)

Text S1: Mechanics of thin nematic elastomer bilayers

We discuss the mechanics of nematic elastomer bilayers and show that the model developed by Agostiniani and DeSimone (*59*) for *thin* nematic elastomer bilayers yields an inverse proportionality between curvature, κ, and thickness, h, in good agreement with in our experimental observations. This relation is observed in our samples (particularly for LT_{NI} hinges), even though the majority of our samples are thick plates. For a more relevant comparison between our experimental results and the calculation of κ discussed below, we highlight the direct proportionality between curvature and hinge angle, θ, in specimens with near-homogeneous curvature (such as ours). Namely, $\theta \approx \kappa w$, where w is hinge width.

Their model is derived based on the condition that there is an isometry constraint on the midplane of thin bilayers due to kinematic frustration (i.e., there is no stretching, and only deformed configurations with zero Gaussian curvature can be achieved). This constraint is an approximation that can be rationalized by contrasting the scaling of stretching and bending energies with regards to plate thickness, h. While the former is linear with h, the latter scales with h^3. This means that bending deformations are heavily favored as structures become increasingly slender, hence the inclusion of the midplane isometry constraint.

Some of the printed LCE hinges are thin and behave in accordance with this regime, but most of our samples are thicker to generate higher torque outputs. In this case, anticlastic bending is observed at the free edges of the hinges, meaning that midplane isometry is not preserved. Because we have limited data on thin LCE actuators, we do not directly compare our results to fittings of parameters used in their model. However, we note that the decreasing curvature with increasing thickness observed in our experiments is characteristic of other bilayer growth systems (*57,58*) and is consistent with the behavior predicted by their model for thin nematic elastomers. We offer an intuition for the mechanics that govern our hinges by summarizing a calculation based on their model, which illustrates that sheet thickness is the characteristic length scale that determines curvature in the thin specimen limit. It is beyond the scope of this study to develop a theory for the curving of thick LCE bilayers.

Kinematics

Denote the coordinate frame for an initially flat midsurface as $\mathbf{X} = \{X, Y\}$. The deformed configuration is $\boldsymbol{\chi} = \{x(X,Y),\ y(X,Y),\ z(X,Y)\}$. The unit-normal to the deformed surface is

$$\mathbf{n} = \frac{\partial \boldsymbol{\chi}}{\partial X} \wedge \frac{\partial \boldsymbol{\chi}}{\partial Y} \Bigg/ \left\| \frac{\partial \boldsymbol{\chi}}{\partial X} \wedge \frac{\partial \boldsymbol{\chi}}{\partial Y} \right\| .$$

The second fundamental form of the midsurfaces is given by:

$$\mathrm{A}_y = -\nabla \boldsymbol{\chi}\ \nabla \mathbf{n} = -\frac{\partial \chi_k}{\partial X_i} \frac{\partial n_k}{\partial X_j}$$

We express this form through the following identity:

$$\nabla \boldsymbol{\chi} \cdot \mathbf{n} = 0 \Rightarrow \nabla(\nabla \boldsymbol{\chi} \cdot \mathbf{n}) = 0$$

In Einstein summation notation, this can be written as:

$$\frac{\partial}{\partial X_j}\left(\frac{\partial \chi_k}{\partial X_i} n_k\right) = 0 \Rightarrow \frac{\partial^2 \chi_k}{\partial X_i \partial X_j} n_k + \frac{\partial \chi_k}{\partial X_i}\frac{\partial n_k}{\partial X_j} = 0 \Rightarrow \mathrm{A}_{ij} = \frac{\partial^2 \chi_k}{\partial X_i \partial X_j} n_k$$

Thus, the second fundamental form can be expressed as follows:

$$\mathrm{A}_y = \begin{bmatrix} \boldsymbol{\chi}_{,XX} \cdot \mathbf{n} & \boldsymbol{\chi}_{,XY} \cdot \mathbf{n} \\ \boldsymbol{\chi}_{,XY} \cdot \mathbf{n} & \boldsymbol{\chi}_{,YY} \cdot \mathbf{n} \end{bmatrix} .$$

At a fixed point on the surface, given an orthonormal tangent vector basis, the principal curvatures are the eigenvalues of A_y.

Summary of the Agostiniani & DeSimone model

Consider a nematic elastomer sheet with a small thickness h_0 and reference configuration domain $\omega^\varepsilon \times (-h_0/2,\ h_0/2)$. The material has a shear modulus $\mu > 0$, energy per unit volume $c > 0$, and a dimensionless material parameter $\alpha_0 > 0$ which couples the magnitude of spontaneous in-plane strains in each layer to the nematic director, n. Taking $(\mathsf{n} \otimes \mathsf{n})\check{}$ as the 2×2 upper left part of $\mathsf{n} \otimes \mathsf{n}$, the symmetric tensor $\check{M}$ is a function of $\alpha_0,\ h_0,\ \mathsf{n}$:

$$\check{M} = \frac{1}{2}\frac{\alpha_0}{h_0}\left[(\mathsf{n} \otimes \mathsf{n})\check{} - \frac{\mathbf{I}_2}{3}\right] ,$$

and is related to the spontaneous linear strain in each layer $\mathbf{E}$ as follows:

$$\check{M} = -\frac{\mathbf{E}}{h_0}.$$

Agostiniani and DeSimone's model for LCE bilayers gives the following functional for the limiting 2D plate theory. The isometric deformation $y \in \mathrm{W}^{2,2}_{\mathrm{iso}} : (\nabla' y)^T \nabla' y = I_2$ which minimizes this functional corresponds to equilibrium.

$$\widehat{\mathscr{F}}^{\varepsilon}_{h_0}(v_{h_0}) \cong \min_{y \in \mathrm{W}^{2,2}_{\mathrm{iso}}(\omega^\varepsilon, \mathbb{R}^3)} \frac{h_0^3}{2} \int_{\omega^\varepsilon} \overline{Q}_2\left(\mathrm{A}_y(x')\right) \mathrm{d}x'$$

In this functional, Here, $\overline{Q}_2$ is a doubly-relaxed energy density that is related to $\check{M}$ through the following set of functions:

- A volumetric term, W_{vol}:

$$W_{vol}(t) = c(t^2 - 1 - 2\log t) \Rightarrow W''_{vol}(t) = 2c\left(1 + \frac{1}{t^2}\right) .$$

- An effective bulk modulus, γ:

$$\gamma := \frac{W''_{vol}(1)}{2\mu + W''_{vol}(1)}. \Rightarrow \gamma = \frac{4c}{2\mu + 4c} .$$

- The relaxed energy density, Q_2:

$$Q_2(D) = 2\mu \left(|\mathbf{sym}(D)|^2 + \gamma\ \mathbf{tr}^2 D\right) ,$$

where $|A| = \sqrt{\mathbf{tr}(AA^T)}$.

- The doubly-relaxed energy density $\overline{Q}_2$:

$$\overline{Q}_2(G) = \frac{1}{12} Q_2\left(G + \frac{3}{2}(\check{M}_1 - \check{M}_2)\right) - \frac{1}{16} Q_2(\check{M}_1 + \check{M}_2).$$

Calculation for an orthogonal bilayer

To compare the results of this model to a *thin* bilayer with same director as our fabricated samples, we consider a bilayer where $\mathsf{n}_1 = (1, 0, 0)$ in the top layer defined by $Z \in [0, h_0/2)$, and $\mathsf{n}_2 = (0, 1, 0)$ in the bottom layer $Z \in (-h_0/2, 0)$. Then,

$$\check{M}_1 = \frac{\alpha_0}{6h_0}\begin{bmatrix} 2 & 0 \\ 0 & -1 \end{bmatrix}, \quad \check{M}_2 = \frac{\alpha_0}{6h_0}\begin{bmatrix} -1 & 0 \\ 0 & 2 \end{bmatrix} .$$

Inserting into the strain energy, we have

$$\overline{Q}_2(\mathrm{A}_y) = \frac{\mu}{72}\left[12\left(a_{11}^2 + a_{22}^2 + \gamma(a_{11} + a_{22})^2\right) + 18\frac{\alpha_0}{h_0}(a_{11} - a_{22}) + \frac{\alpha_0^2(13 - \gamma)}{h_0^2}\right] ,$$

where a_{ij} are the elements of A_y. We seek to minimize

$$\widehat{\mathscr{F}}^{\varepsilon}_{h_0}(v_{h_0}) \cong \min_{y \in \mathrm{W}^{2,2}_{\mathrm{iso}}(\omega^\varepsilon, \mathbb{R}^3)} \frac{h_0^3}{2} \int_{\omega^\varepsilon} \overline{Q}_2\left(\mathrm{A}_y(x')\right) \mathrm{d}x'$$

under the constraint of isometric deformations $y \in \mathrm{W}^{2,2}_{\mathrm{iso}} : (\nabla' y)^T \nabla' y = I_2$ over the entire domain. The sheet's flat initial configuration, nematic order symmetry, and the isometric deformation constraint require solutions of the form

$$\mathrm{A}_y = \begin{bmatrix} k & 0 \\ 0 & 0 \end{bmatrix} \text{ or } \mathrm{A}_y = \begin{bmatrix} 0 & 0 \\ 0 & k \end{bmatrix}$$

The boundary conditions impose $y_{,YY} \cdot \mathbf{n} = 0$ at the edges located at $X = 0$ and $X = \epsilon$ (in the reference configuration), so we restrict ourselves to deformations which result in curvatures of the form

$$\mathrm{A}_y = \begin{bmatrix} k & 0 \\ 0 & 0 \end{bmatrix}$$

Assuming homogeneous curvature in the deformed configuration, the minimization problem becomes:

$$\widehat{\mathscr{F}}^{\varepsilon}_{h_0}(v_{h_0}) \cong \min_{y \in \mathrm{W}^{2,2}_{\mathrm{iso}}(\omega^{\varepsilon}, \mathbb{R}^3)} \frac{\mu|\omega^{\epsilon}|h_0}{144}\left(12h_0^2(1+\gamma)k^2 + 18\alpha_0 h_0 k + (13-\gamma)\alpha_0^2\right)$$

This has the solution

$$\widehat{\mathscr{F}}^{\varepsilon}_{h_0}(v_{h_0}) \cong \frac{\mu\alpha_0^2|\omega^{\epsilon}|h_0\big(25 + 4\gamma(12-\gamma)\big)}{576(1+\gamma)}$$

with

$$k = -\frac{3\alpha_0}{4(1+\gamma)h_0}$$

Since $\gamma = 4c/(2\mu + 4c)$, we get:

$$k = -\frac{3\alpha_0(2c+\mu)}{(16c+4\mu)h_0}$$

Remembering that α_0, c and μ are material parameters, this is consistent with the inverse proportionality between curvature and thickness that is observed in many systems with differential growth across bilayers, including our experiments. We remind the reader that hinge angle is directly proportional to curvature for homogeneously-curved specimens. As such, the Agostiniani & DeSimone model predicts the following relation between hinge angle and thickness for thin LCEs:

$$\theta \propto \frac{1}{h_0}$$

Our experiments show that this prediction may extend to thicker specimens. We believe this model provides an intuition for the mechanics that govern our hinges, but note that the observation of anticlastic bending in our thicker samples shows that the isometric assumption should not be maintained in a rigorous theory for thick LCE bilayers.

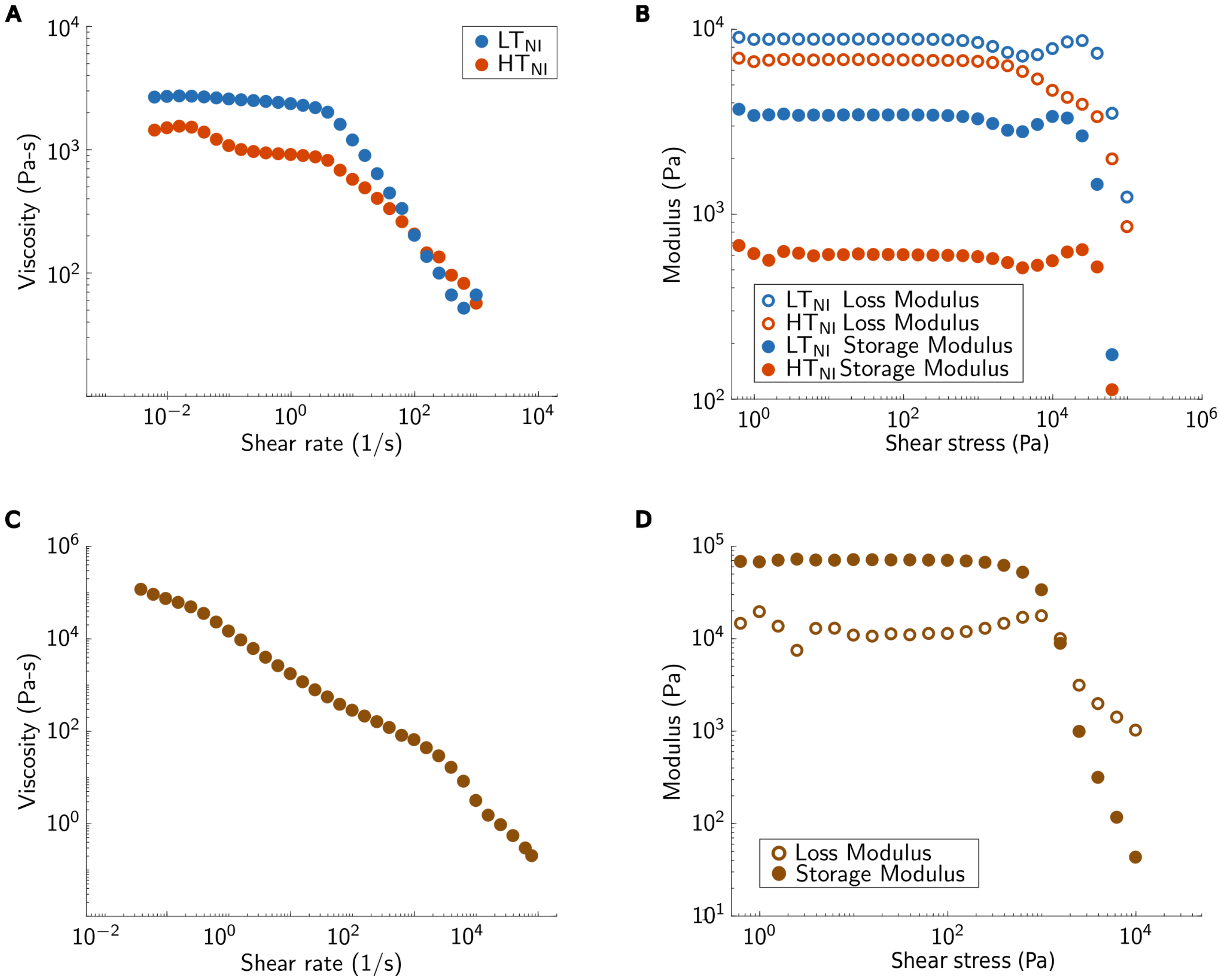

Figure S1. LCE and structural tile ink rheology. (**A**) Apparent viscosity as a function of shear rate for LT_{NI} and HT_{NI} LCE inks at printing temperature 26°C and 55°C, respectively. (**B**) Storage (G') and loss (G'') moduli as a function of shear stress at 1 Hz for LT_{NI} and HT_{NI} LCE inks at the respective printing temperatures of 26°C and 55°C. (**C**) Apparent viscosity as a function of shear rate for the structural polymer ink under ambient conditions. (**D**) Storage (G') and loss (G'') moduli as a function of shear stress at 1 Hz for the structural polymer ink under ambient conditions.

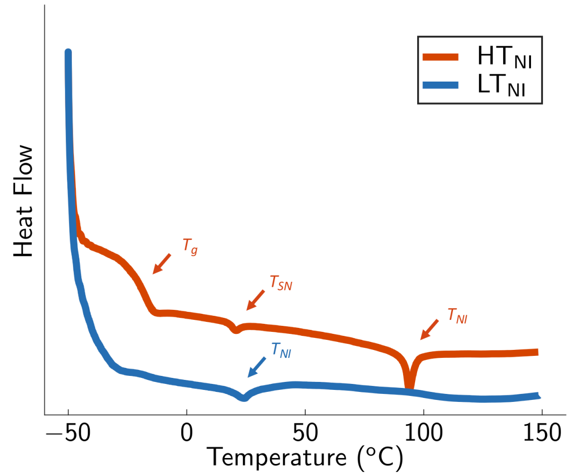

Figure S2. Differential scanning calorimetry curves for the LCE inks. The two oligomeric LCE inks exhibit LT_{NI} and HT_{NI} values of approximately 24°C and 94°C, respectively. [Note: From this data, the T_g and smectic-to-nematic transition temperature (T_{SN}) for the HT_{NI} ink are approximately -20 °C and 20 °C, respectively.]

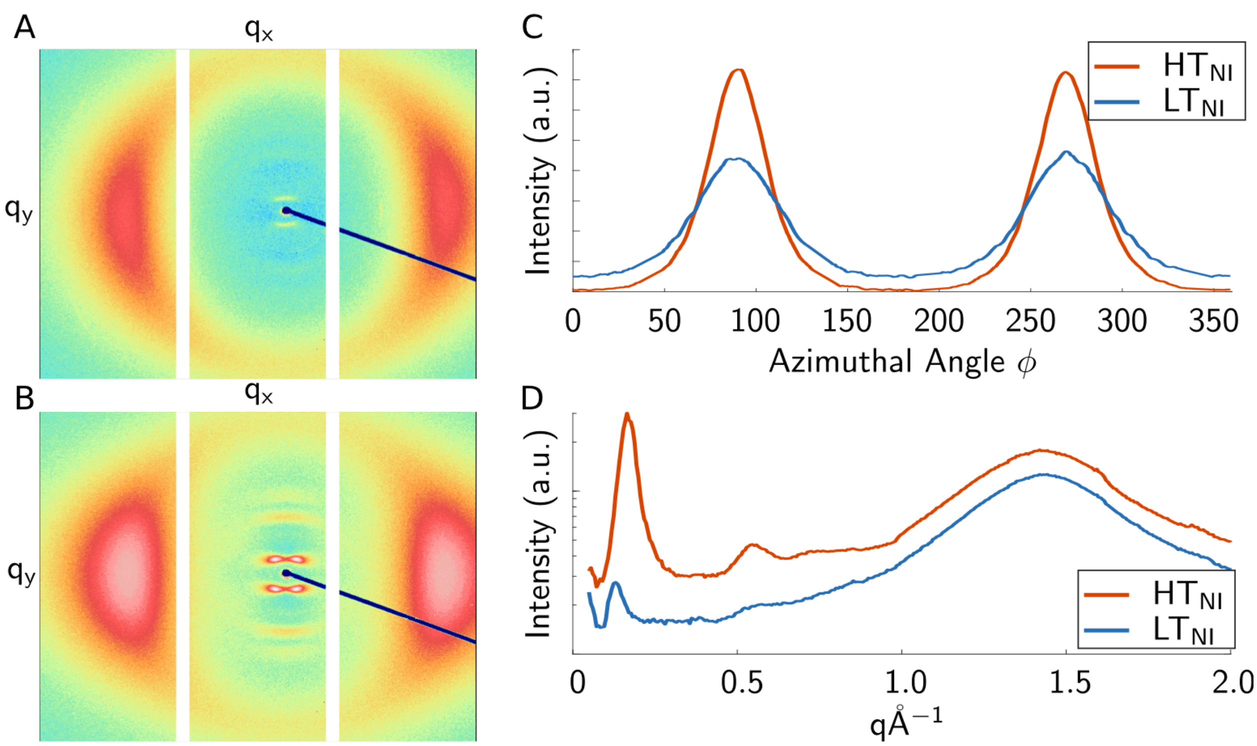

Figure S3. **LCE alignment.** 2D wide angle X-Ray scattering patterns of unidirectional printed (**A**) LT_{NI} and (**B**) HT_{NI} LCEs. (**C**) Normalized intensity as a function of azimuthal angle. (**D**) Normalized radial intensity as a function of the momentum transfer vector $q = (4\pi/\lambda) \sin \theta$.

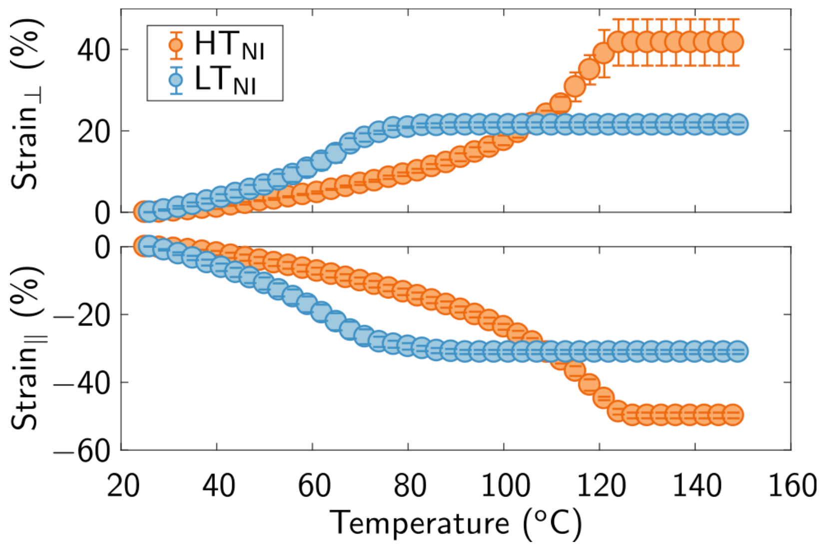

Figure S4. Actuation response of unidirectional printed LCEs. The measured contractile and expansion strain observed perpendicular and parallel to the print direction, respectively, as a function of temperature for unidirectional aligned LCE actuators printed from LT_{NI} and HT_{NI} inks [Note: Sample dimensions are approximately 20 mm x 5 mm x 0.375 mm.]

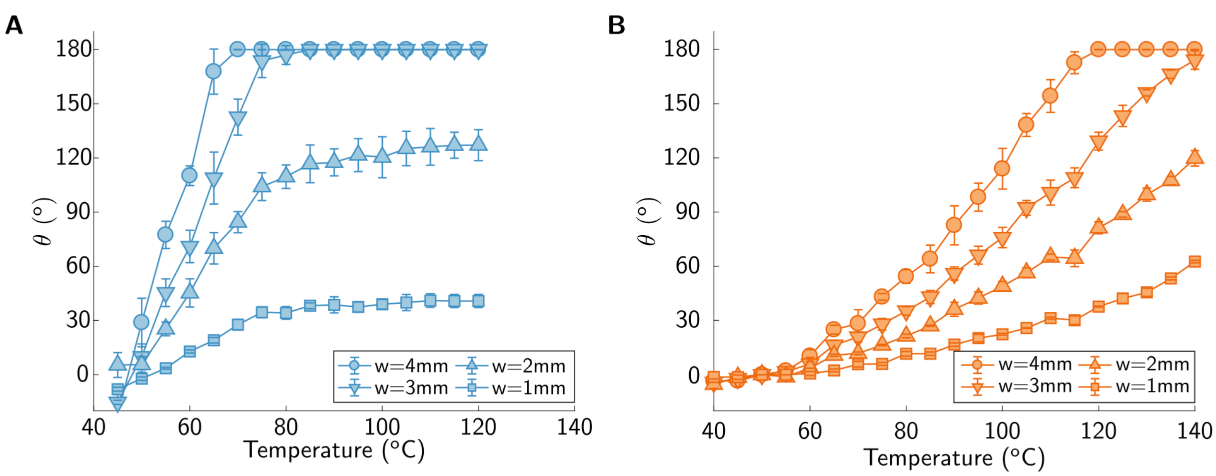

Figure S5. Bending angle as a function of temperature. Bending angles θ of (**A**) LT_{NI} and (**B**) HT_{NI} LCE hinges (0.25 mm thick) with varying width (*w*=1-4 mm) as a function of temperature. Due to residual stress that arises from printing and cross-linking the LT_{NI} LCE hinges in the isotropic phase, their measured bending angle is negative at low temperatures.

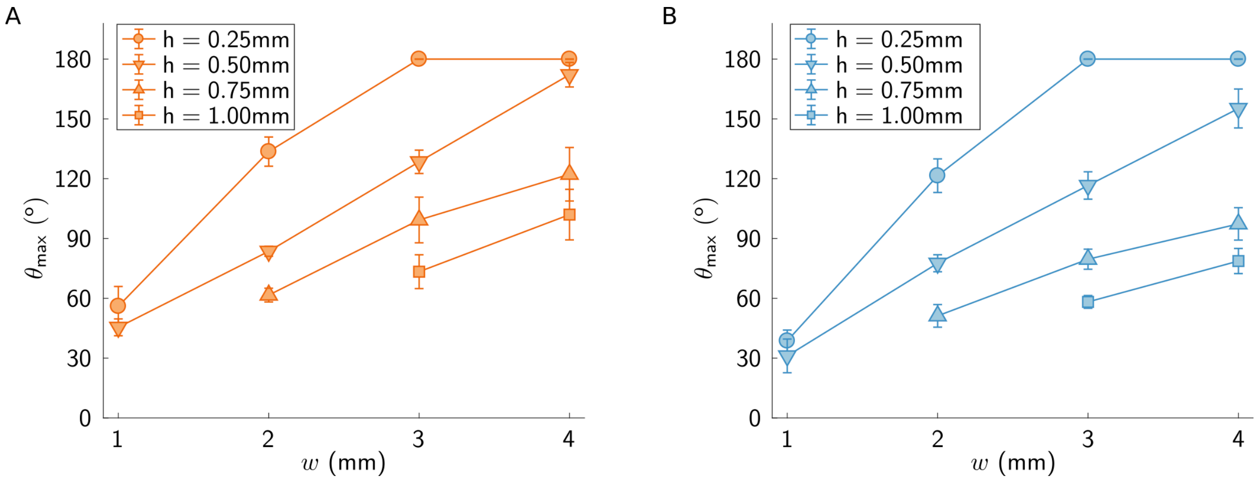

Figure S6. Bending angle as a function of hinge dimensions. Bending angles of LCE hinges of varying thickness (h) and width (w), when actuated above their T_{NI}. Hinge angles θ are measured at 120°C and 150°C for the LT_{NI} and HT_{NI} LCE hinges, respectively. Maximum bending angle is 180° due to panel collision.

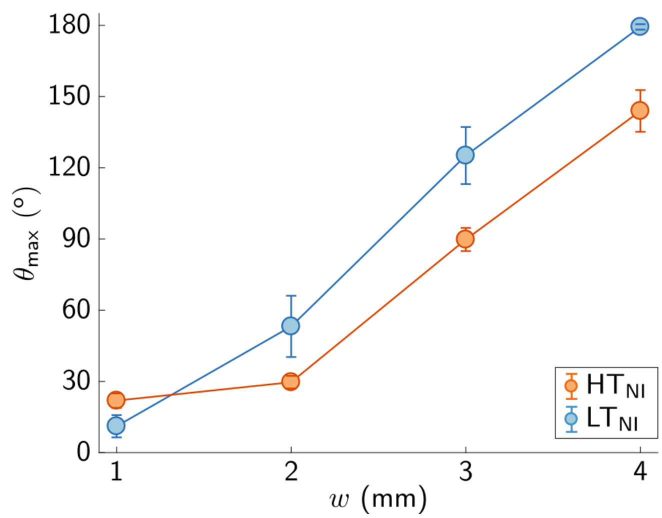

Figure S7. Valley fold bending angles. Printed LCE hinges (0.25 mm thick) of varying width w exhibit valley folds with smaller bending angles θ than their mountain fold counterparts.

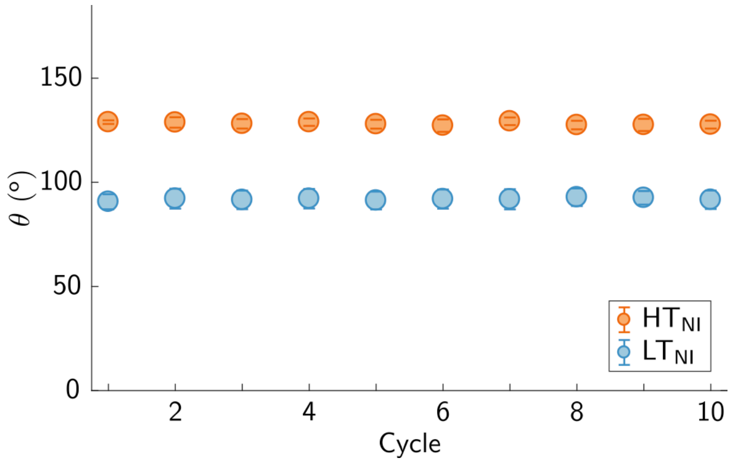

Figure S8. Repeatable hinge folding. Bending angles θ of LT_{NI} and HT_{NI} LCE hinges (0.25 mm thick and 2 mm wide) when cycled above and below T_{NI}.

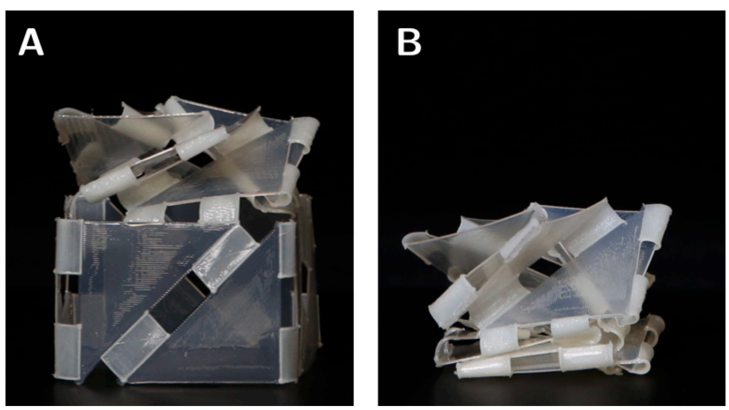

Figure S9. Triangulated polyhedron actuation sequence at ambient temperature. (**A**) The triangulated polyhedron in its second, partially folded configuration after heating to actuate the top LT_{NI} section. (**B**) The triangulated polyhedron in its third, fully folded configuration after heating to actuate the bottom HT_{NI} section. All images are taken under ambient conditions.

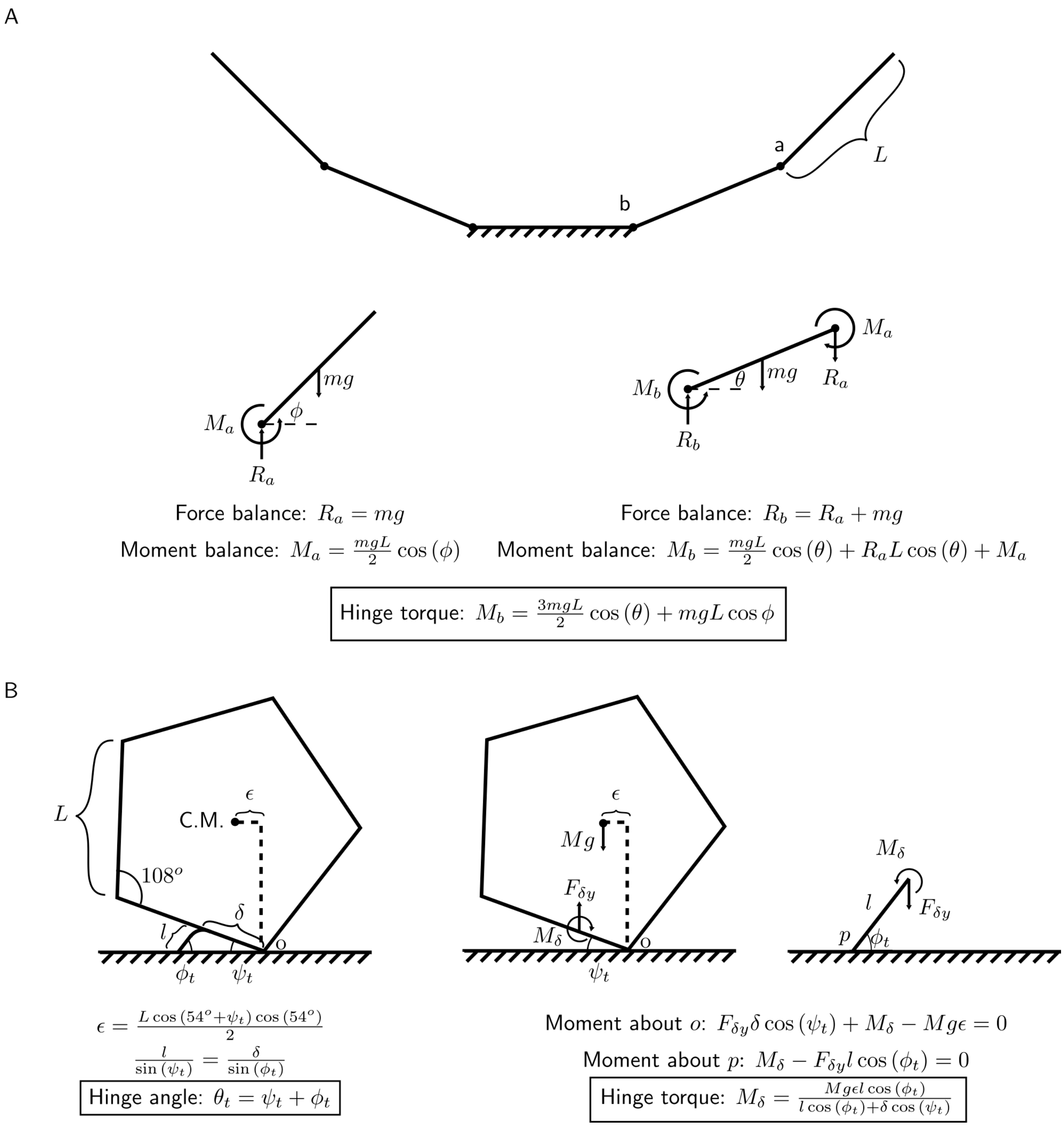

Figure S10. Free body diagrams of self-propelling rollbot. (**A**) Moment diagrams for calculating the torque at the LT_{NI} LCE hinge (b) that requires the greatest torque for self-reconfiguration into a pentagonal prism. Here, *m* is the mass of each panel, *g* is gravitational acceleration, *L* is the length of each panel. (**B**) Moment diagrams for calculating the torque requirements of HT_{NI} LCE hinges that induce self-propulsion. Here, *M* is the entire mass of the structure, *ε* is the offset of the center of mass *C.M.* from the tipping point, *l* is the length of the propelling plate, *δ* is the offset of the hinge from the tipping vertex, *o*. A no-friction assumption is taken for the contact between the structure and the ground. Only forces that affect a torque about the tipping point are shown for clarity in the image.

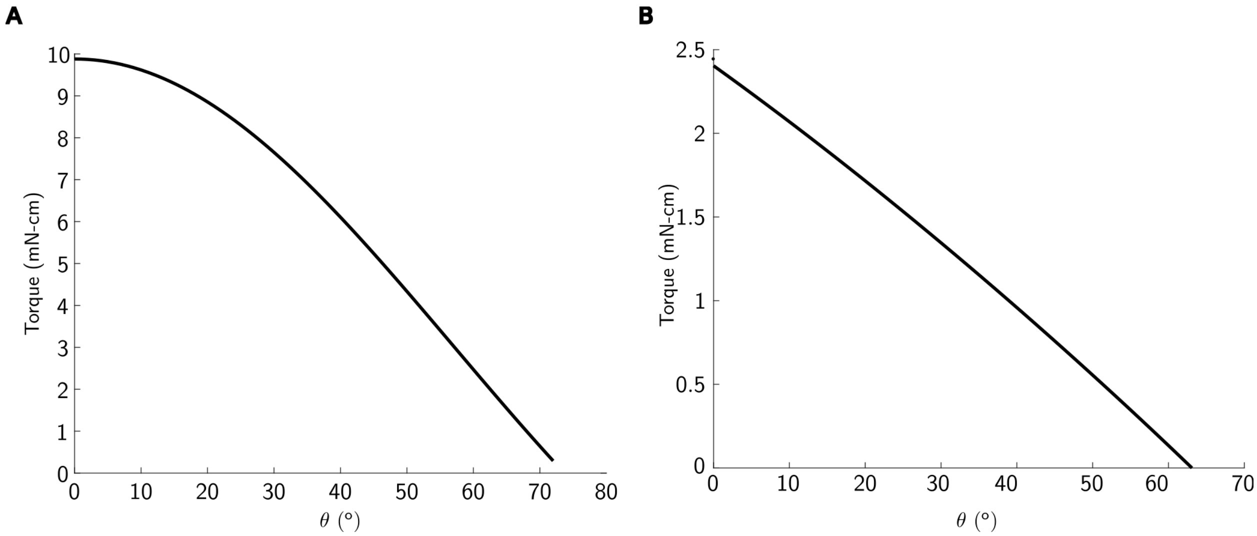

Figure S11. Torque requirements of hinges for self-propelling rollbot. (**A**) Torque required from LT_{NI} LCE hinges for self-assembly into a pentagon as a function of folding angle θ. (**B**) Torque required from HT_{NI} LCE hinges as a function hinge angle for self-propulsion. The required moment is zero at the tipping point. A 63° hinge angle induces a 36° tipping angle about the vertex.

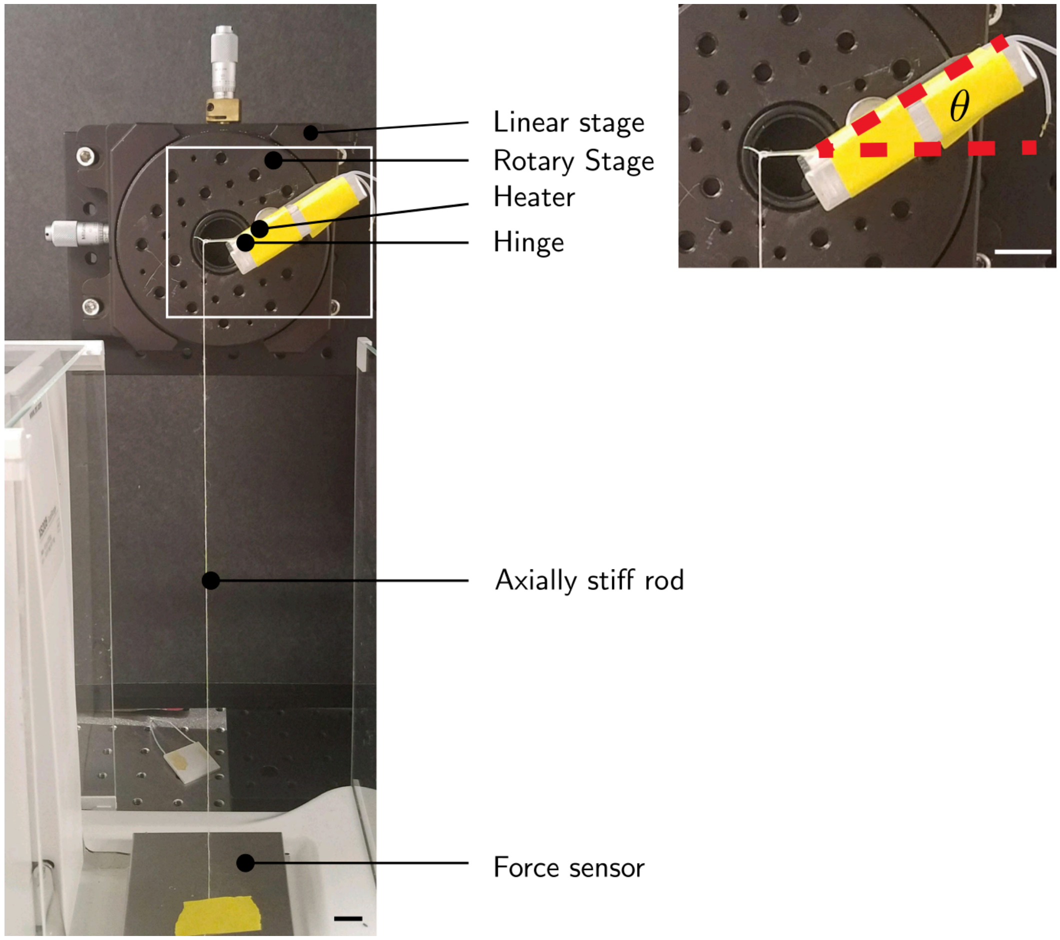

Figure S12. Torque measurement experimental setup. Torque of the LCE hinges can be measured (left) as a function of angle θ by rotating a rotary stage (right). The force sensor is attached to the hinge at the end of the panel, approximately 1 cm from the edge of the LCE component, which is in contact with a thin heater. A linear stage is used to ensure that the hinge tile attached to the force sensor is parallel to the sensor surface. Scale bars are 1 cm.

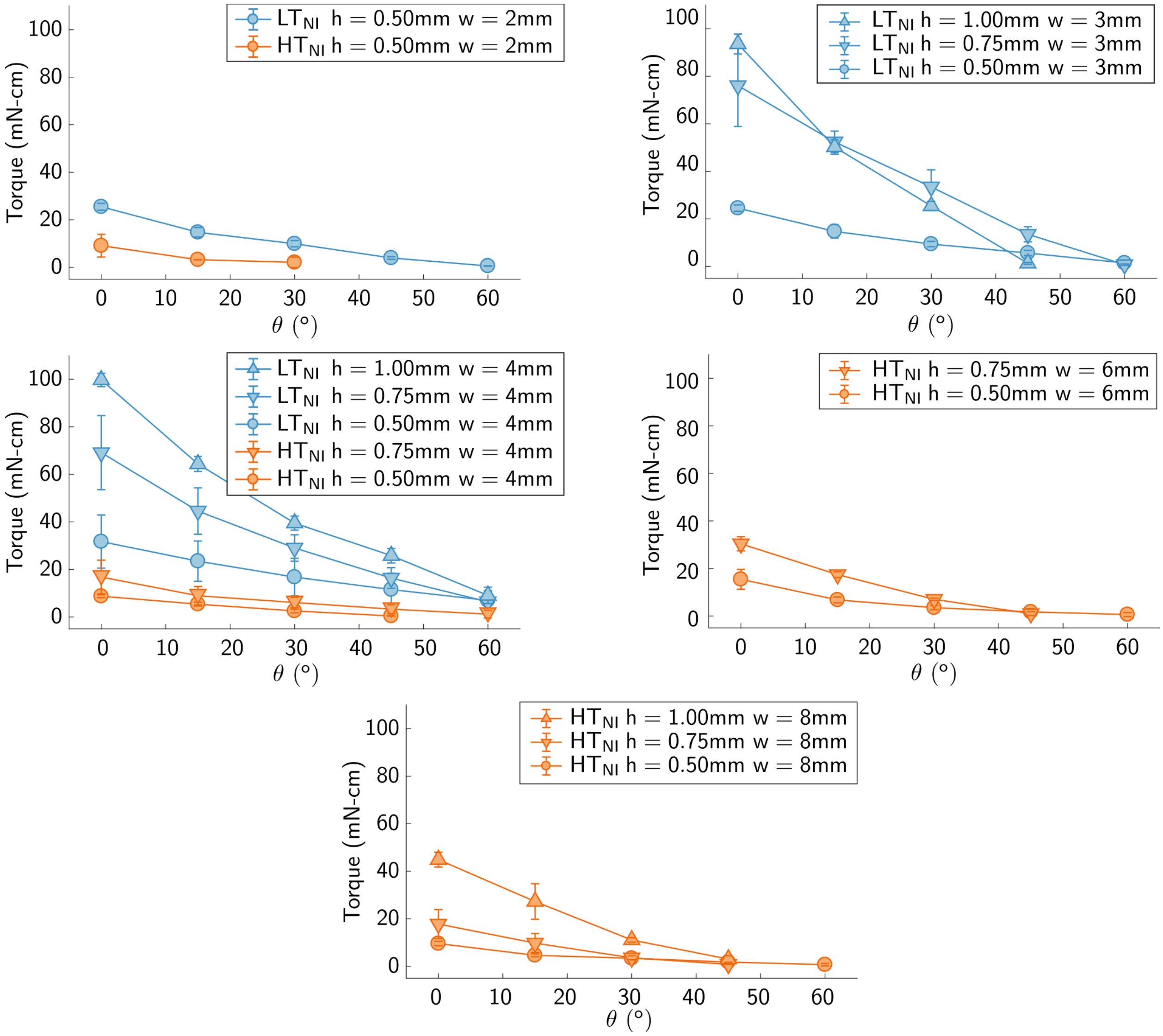

Figure S13. Torque measurements for hinges of varied dimensions. *h* indicates hinge thickness in mm, *w* indicates hinge width in mm, and θ is the folding angle.